ADVANCES IN ATMOSPHERIC SCIENCES, 2024

• Original Paper •

Distribution and Formation Causes of $PM_{2.5}$ and O_3 Double High Pollution Events in China during 2013–20

Zhixuan TONG[1], Yingying YAN[*1,2], Shaofei KONG[1,3], Jintai LIN[4], Nan CHEN[1,3], Bo ZHU[3,5], Jing MA[1,6], Tianliang ZHAO[7], and Shihua QI[1,8]

[1]*Department of Atmospheric Science*, *School of Environmental Sciences*, *China University of Geosciences*, *Wuhan* 430074, *China*

[2]*State Key Laboratory of Atmospheric Boundary Layer Physics and Atmospheric Chemistry*, *Institute of Atmospheric Physics*, *Chinese Academy of Sciences*, *Beijing* 100029, *China*

[3]*Research Centre for Complex Air Pollution of Hubei Province*, *Wuhan* 430074, *China*

[4]*Laboratory for Climate and Ocean–Atmosphere Studies*, *Department of Atmospheric and Oceanic Sciences*, *School of Physics*, *Peking University*, *Beijing* 100871, *China*

[5]*Eco-Environmental Monitoring Centre of Hubei Province*, *Wuhan* 430074, *China*

[6]*Key Laboratory of Atmospheric Chemistry*, *China Meteorological Administration*, *Beijing* 100081, *China*

[7]*School of Atmospheric Physics*, *Nanjing University of Information Science and Technology*, *Nanjing* 210044, *China*

[8]*State Key Laboratory of Biogeology and Environmental Geology*, *China University of Geosciences*, *Wuhan* 430074, *China*

(Received 18 July 2023; revised 24 October 2023; accepted 9 November 2023)

ABSTRACT

Fine particulate matter ($PM_{2.5}$) and ozone (O_3) double high pollution (DHP) events have occurred frequently over China in recent years, but their causes are not completely clear. In this study, the spatiotemporal distribution of DHP events in China during 2013–20 is analyzed. The synoptic types affecting DHP events are identified with the Lamb–Jenkinson circulation classification method. The meteorological and chemical causes of DHP events controlled by the main synoptic types are further investigated. Results show that DHP events (1655 in total for China during 2013–20) mainly occur over the North China Plain, Yangtze River Delta, Pearl River Delta, Sichuan Basin, and Central China. The occurrence frequency increases by 5.1% during 2013–15, and then decreases by 56.1% during 2015–20. The main circulation types of DHP events are "cyclone" and "anticyclone", accounting for over 40% of all DHP events over five main polluted regions in China, followed by southerly or easterly flat airflow types, like "southeast", "southwest", and "east". Compared with non-DHP events, DHP events are characterized by static or weak wind, high temperature (20.9°C versus 23.1°C) and low humidity (70.0% versus 64.9%). The diurnal cycles of meteorological conditions cause $PM_{2.5}$ (0300–1200 LST, Local Standard Time= UTC+ 8 hours) and O_3 (1500–2100 LST) to exceed the national standards at different periods of the DHP day. Three pollutant conversion indices further indicate the rapid secondary conversions during DHP events, and thus the concentrations of NO_2, SO_2 and volatile organic compounds decrease by 13.1%, 4.7% and 4.4%, respectively. The results of this study can be informative for future decisions on the management of DHP events.

Key words: double high pollution events, $PM_{2.5}$, ozone, spatiotemporal distribution, meteorological causes, chemical composition characteristics

Citation: Tong, Z. X., and Coauthors, 2024: Distribution and formation causes of $PM_{2.5}$ and O_3 double high pollution events in China during 2013–20. *Adv. Atmos. Sci.*, https://doi.org/10.1007/s00376-023-3156-9.

Article Highlights:

- The spatiotemporal distribution of DHP events in China during 2013–20 is analyzed.
- The synoptic types affecting DHP events are identified with the Lamb–Jenkinson circulation classification method.
- The diurnal cycles of meteorological conditions cause $PM_{2.5}$ and ozone to exceed the national standards at different periods of the DHP day.
- The secondary conversions of NO_2, SO_2 and VOCs were signicantly intensified during DHP events.

* Corresponding author: Yingying YAN
Email: yanyingying@cug.edu.cn

1. Introduction

China has been combating air pollution since the 21st century (Huang et al., 2014a), of which fine particulate matter ($PM_{2.5}$) and surface ozone (O_3) cause hazards related to atmospheric visibility, human health, climate, and agriculture (Brauer et al., 2016; Wang et al., 2017, 2021; Zhao et al., 2017; Fleming et al., 2018; Mills et al., 2018). Previous studies have shown that both $PM_{2.5}$ and O_3 concentrations show a monthly pattern. The highest concentration of $PM_{2.5}$ in China occurs in January or February, with a small peak in May–July, a stable level in June–September, and a gradual increase in October–December (Wang et al., 2015; Shi et al., 2022). Meanwhile, studies on O_3 show that warmer periods (April–September, with meteorological conditions as the main influencing factor) are most favorable for increases in O_3 concentrations (Ding et al., 2013; Lu et al., 2018; Liu et al., 2020). Thus, there is possibly a period when the concentrations of $PM_{2.5}$ and O_3 are both at high values.

The sources of $PM_{2.5}$ can be divided into direct emission sources (organic carbon, elemental carbon, heavy metals, etc.) and secondary sources (secondary organic and inorganic aerosols) (Huang et al., 2014b; Wang et al., 2019). Surface O_3 is the secondary product of photochemical reactions of carbon monoxide (CO) and volatile organic compounds (VOCs) in the presence of nitrogen oxides (NO_x) by the oxidation of hydroxyl radicals (Monks et al., 2015; Yan et al., 2021a). Due to their common precursors of NO_x and VOCs, the secondary components of $PM_{2.5}$ and O_3 are intricately linked and interact with each other through photochemical and heterogeneous pathways, leading to a complex nonlinear response (Qian et al., 2019; He et al., 2022b). Thus, so-called "double high pollution" (DHP) events, which are caused by both $PM_{2.5}$ [daily average > 75 μg m^{-3}; NAAQS (National Ambient Air Quality Standard) Grade II standards] and O_3 [MDA8 (maximum daily 8-h average) > 160 μg m^{-3}; NAAQS Grade II standards], have been gradually drawing attention (Qin et al., 2021).

In recent years, following China issuing its Air Pollution Prevention and Control Action Plan (2013) and Three-Year Action Plan (2018) to control anthropogenic precursor emissions, the annual average concentrations and exceedance rates of $PM_{2.5}$ in China have shown a significant decreasing trend (Li et al., 2019a, b; Zhai et al., 2019; Zhao et al., 2021). From 2013 to 2017, anthropogenic emissions of sulfur dioxide (SO_2), NO_x, CO, ammonia (NH_3), black carbon, and organic carbon (OC) in China decreased by 59%, 21%, 23%, 3%, 28%, and 32%, respectively (Zheng et al., 2018). However, the annual average $PM_{2.5}$ concentration in 2019 was still 1.11 times higher than the secondary National Ambient Air Quality Standard (GB 3095–2012) (35 μg m^{-3}) (Shi et al., 2022). In contrast, due to less attention paid to pollutants such as VOCs (Lin et al., 2018), O_3 concentrations in China continued to rise until 2020 (Li et al., 2020; Zhao et al., 2021; He et al., 2022b). From 2013 to 2017, the maximum daily average concentration of O_3 in the 90th percentile of China increased from 137.2 to 169.4 μg m^{-3} (Wang et al., 2020). The maximum MDA8 O_3 concentration reached 276.1 μg m^{-3} in summer 2019, with average MDA8 O_3 concentrations of 177.6, 143.4, 98.4, and 122.0 μg m^{-3} over the North China Plain (NCP), Yangtze River Delta (YRD), Pearl River Delta (PRD), and Sichuan Basin (SCB), respectively (Li et al., 2020). As a result, DHP events have occurred frequently over China in recent years.

However, reports of DHP events in China are still few. Dai et al. (2021) found that over the YRD, during 2013–19, there were a total of 54 days of DHP in Shanghai and 71 days in Jiangsu Province, which were primarily observed during the months of April, May, June, and October. He et al. (2022a) found that the maximum hourly average concentrations of O_3 and $PM_{2.5}$ reached up to 190 and 98 μg m^{-3}, respectively, over the PRD on 6–7 December 2020. Zong et al. (2021) reported that the number of days of DHP events over eastern China was 85 during 2015–18. Nevertheless, these recent studies mainly focused on DHP events (or a single DHP event in a short period of time) over the Beijing–Tianjin–Hebei, YRD, and PRD regions, but did not systematically elaborate on the spatiotemporal distribution of DHP events in China during their respective study periods.

As we know, apart from the impact of emissions, meteorological conditions and synoptic climate systems have an important effect on the formation of $PM_{2.5}$ and O_3 pollution (Hou et al., 2019; Zhao et al., 2020). During $PM_{2.5}$ pollution, meteorological conditions are often characterized by still or weak winds, high relative humidity, and temperature inversion, while O_3 pollution is often controlled by strong radiation, still winds, low relative humidity, and high temperatures (Chen et al., 2020a; Zhao et al., 2020; Ma et al., 2021). Current studies have shown that, during DHP events, temperature is positively correlated with O_3 concentration but negatively correlated with $PM_{2.5}$ concentration. In addition, relative humidity and sea level pressure (SLP) show weak negative correlation with O_3 concentration and weak positive correlation with $PM_{2.5}$ concentration (Qin et al., 2021). Dai et al. (2021) showed that, in the YRD, the occurrence of DHP events mainly depends on low relative humidity, high temperatures, and low wind speeds, and their average anomalies during DHP events were found to be −6.2%, 1.84°C, and −0.40 m s^{-1}, respectively. He et al. (2022a) found that the co-occurrence of $PM_{2.5}$ and O_3 pollution resulted from the arrival of a cold front over the PRD, within which meteorological and transport factors played a significant role in the formation of DHP. Zong et al. (2021) found that DHP events over eastern China during summer had a close relationship with the western Pacific subtropical high (WPSH). The probabilities of DHP at all sites under the resolved four types classified with the T-mode PCA method were 54.3%, 33.8%, 6.8%, and 5.1%, respectively. However, the causes of DHP events are not completely clear. There is a lack of research on the relationship and effects of the two pollutants in terms of chemical components, which is insufficient to fully understand DHP events.

In the present paper, to clarify the distribution and forma-

tion causes of DHP events in China, we analyze the spatial and temporal distribution characteristics of DHP events during 2013–20 using observational data of $PM_{2.5}$ and surface O_3. Then, employing the Lamb–Jenkinson circulation classification method, we further classify the main circulation types of DHP events and their meteorological effects on DHP events over five main polluted regions in China. Finally, the chemical composition characteristics and their meteorological causes during DHP events are discussed over Central China (CC). This region is geographically surrounded by the major haze pollution regions of the NCP, YRD, PRD, and SCB (Fig. 1), thereby acting as a regional hub for pollutant transport due to its sub-basin topography (Yan et al., 2021b). The motivation behind this study is to provide an insightful view for better understanding the co-occurrence of O_3 and $PM_{2.5}$ pollution over China. Moreover, the results can help in establishing pollution prevention plans for DHP events within China and benefit the country's fore-

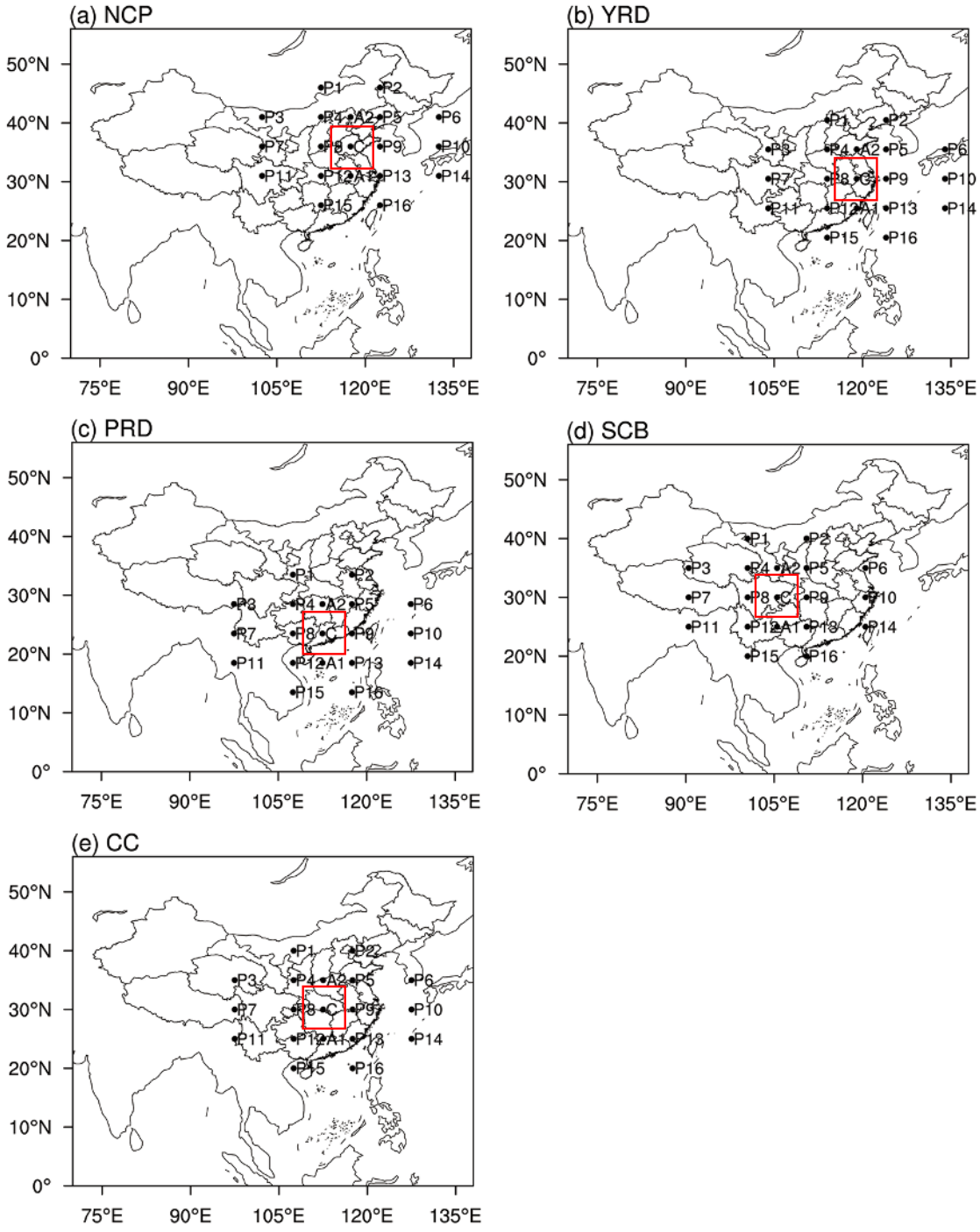

Fig. 1. Locations of five main polluted regions (NCP, YRD, PRD, SCB, CC) and the grid points used in Lamb–Jenkinson circulation classification.

cast and policy decisions on future air pollution control.

2. Data and methods

2.1. *Data and the criteria used to identify and define DHP*

Hourly in situ observational data (2013–20) were obtained from China's Ministry of Ecology and Environment (https://air.cnemc.cn/; last accessed 11 October 2021) and archived at https://quotsoft.net/air (Wang, 2021; last accessed 30 June 2021). The network was launched in 2013 as part of the Clean Air Action Plan. It included 944 monitoring stations in 2013, which since grew to around 1700 stations by 2020. $PM_{2.5}$ and O_3 concentrations are measured across all of the sites with the same maintenance and calibration criteria. In order to identify DHP events, we applied hourly $PM_{2.5}$ concentration data and O_3 8-h sliding average (O_3_8h) data to calculate the daily mean $PM_{2.5}$ ($PM_{2.5}$_24h) and the maximum O_3_8h in a day (O_3_8h_24h), respectively. We then defined a DHP event as the calculated values ($PM_{2.5}$_24h and O_3_8h_24h) of any station in China exceeding the DHP standard ($PM_{2.5}$_24h > 75 μg m^{-3} and O_3_8h_24h > 160 μg m^{-3}).

We downloaded hourly mean SLP (MSLP) data (for circulation classification) and hourly meteorological data at different altitudes (to analyze the meteorological conditions of the classified circulation types) from 2013 to 2020 published by ECMWF (ERA5 reanalysis; 0.25° latitude × 0.25° longitude; https://www.ecmwf.int/en/forecasts/dataset/ecmwf-reanalysis-v5/, last accessed 4 December 2021). The data include total precipitation and total sky direct solar radiation at surface level, temperature and relative humidity at 1000 hPa, and geopotential height and wind field at 850 hPa and 500 hPa. ERA5 replaced ERA-Interim as the ECMWF's major reanalysis product and is based on the Integrated Forecasting System Cy41r2, which became operational in 2016. ERA5 thus benefits from a decade of developments in model physics, core dynamics, and data assimilation (Hersbach et al., 2020).

The observed hourly meteorological data and chemical components of DHP events over Wuhan were obtained from the Hubei Atmospheric Superstation Network Integrated Analysis Platform (http://59.172.208.250:8082/, last accessed on March 21, 2022). The meteorological data cited in the analysis include visibility, relative humidity, temperature, air pressure, and wind field. The chemical species mainly include the precursors and chemical components of $PM_{2.5}$ and O_3, such as NO_2, SO_2, secondary inorganic aerosols (SIAs), carbonaceous substances, and crustal elements.

2.2. *Lamb–Jenkinson circulation classification method*

The Lamb–Jenkinson circulation classification method is an objective approach obtained by Jenkinson and Collison (1977) on the basis of the subjective typing method of Lamb (1950) by defining indices and classification criteria. This method combines both subjective and objective classification methods, which can eliminate the inaccuracy of subjective judgment and combine the experience of subjective judgment on the basis of objective analysis, making the classification results more accurate and generalized (Huang et al., 2016). The Lamb–Jenkinson circulation classification method has clear weather and climatology significance, and has been adopted in a large number of studies in meteorological science and climate change (Liu et al., 2019).

In this study, we separately take the centers of the latitude and longitude ranges of the NCP (117.5°N, 36°E), YRD (119°N, 30.5°E), PRD (112.5°N, 23.5°E), SCB (105.5°N, 30°E), and CC (112.5°N, 30°E) and designate them as the C point during circulation classification, and take a total of 16 grid points every 5° latitude and 10° longitude (Fig. 1). After taking out the 16 grid points, we substitute the daily MSLP of each grid point through the central differential calculation scheme to obtain the following six circulation indices:

$$u = 0.5[P(12) + P(13 - P(4) - P(5))] , \tag{1}$$

$$v = \frac{1}{\cos\alpha} \times \frac{1}{4}[P(4) + 2P(9) + P(13) - P(4) - 2P(8) - P(12)] , \tag{2}$$

$$V = \sqrt{u^2 + v^2} , \tag{3}$$

$$\psi_u = \frac{\sin\alpha}{2\sin\alpha_1}[P(15) + P(16) - P(8) - P(9)] - \frac{\sin\alpha}{2\sin\alpha_2}[P(8) + P(9) - P(1) - P(2)] , \tag{4}$$

$$\xi_V = \frac{1}{8\cos^2\alpha}[P(6) + 2P(10) + P(14) - P(5) - 2P(9) - P(13) + P(3) + 2P(7) + P(11) - P(4) - 2P(8) - P(12)] , \tag{5}$$

$$\xi = \xi_u + \xi_v , \tag{6}$$

where $P(n)$ (n = 1, 2, ... ,16) denotes the SLP at grid point n; α, α_1 and α_2 represent the latitude values of points C, A1 and A2, respectively; V represents the geostrophic wind; u and v represent its latitudinal and longitudinal components, respectively; ξ represents the geostrophic vorticity; ξ_u represents the longitudinal gradient of u; and ξ_v represents the latitudinal gradient of v, in hPa per 10° longitude.

According to the relationship between the magnitude of circulation indices, we divide the circulation types into 3 major categories and 26 types, as shown in Table 1.

2.3. *Pollutant conversion indices*

SOR and NOR indicate the conversion rates of the precursors SO_2 and NO_2 to the SIAs SO_4^{2-} and NO_3^-, respec-

Table 1. Lamb–Jenkinson circulation types.

$\lvert\xi\rvert \leqslant V$ (flat airflow type)	$\lvert\xi\rvert \geqslant 2V$ (rotating airflow type)	$V \leqslant \lvert\xi\rvert \leqslant 2V$ (mixed type)
N (north)	C (cyclone)	CN (cyclone–north), CE (cyclone–east)
E (east)	A (anticyclone)	CS (cyclone–south), CW (cyclone–west)
S (south)		CNE (cyclone–northeast)
W (west)		CSE (cyclone–southeast)
NE (northeast)		CSW (cyclone–southwest)
SE (southeast)		CNW (cyclone–northwest)
SW (southwest)		AN (anticyclone–north), AE (anticyclone–east)
NW (northwest)		AS (anticyclone–south), AW (anticyclone–west)
		ANE (anticyclone–northeast)
		ASE (anticyclone–southeast)
		ASW (anticyclone–southwest)
		ANW (anticyclone–northwest)

tively. Both indices can be used to express the conversion efficiency of primary to secondary pollutants (Qin et al., 2021), and the expressions of NOR and SOR are as follows:

$$\mathrm{NOR} = \frac{\left[\mathrm{NO_3^-}\right]}{\left[\mathrm{NO_3^-}\right] + \left[\mathrm{NO_2}\right]}, \tag{7}$$

$$\mathrm{SOR} = \frac{\left[\mathrm{SO_4^{2-}}\right]}{\left[\mathrm{SO_4^{2-}}\right] + \left[\mathrm{SO_2}\right]}, \tag{8}$$

where $[NO_3^-]$, $[NO_2]$, $[SO_4^{2-}]$ and $[SO_2]$ represent the concentrations of these four substances in mol m^{-3}.

OC/EC (organic carbon/elemental carbon) is used to indicate the emission and conversion rate of carbonaceous aerosols. When the value of OC/EC is greater than 2, it indicates the presence of secondary organic carbon in the atmosphere (Huang et al., 2019; Qin et al., 2021).

3. Results

3.1. *Spatiotemporal distribution of DHP events over China*

As shown in Fig. 2, the occurrence frequency (region) of DHP events in China increases year by year from 2013 to 2015 (2013 to 2018). The enhancements over the NCP, YRD, PRD, and SCB regions are the most obvious. In addition, the occurrence of DHP events over CC is also extensive, probably owing to its topography and the transmission process with its surrounding regions (Yan et al., 2021b). However, DHP events show a decreasing trend after the year 2015. During the study period, the annual occurrence frequencies of DHP events over the NCP, YRD and PRD are more than six times per site (Fig. 2). This can possibly be attributed to high concentrations of primary pollutants emitted by industry and agriculture over these main economic development zones in China, and the unfavorable geographical and meteorological conditions (Wang et al., 2015; Li et al., 2020; Shi et al., 2022). Wang et al. (2015) showed that, during 2013–14, the regions with severe $PM_{2.5}$ pollution were over the NCP, the middle and lower Yangtze River Plain, and the SCB. Shi et al. (2022) also showed that, in 2015–19, the locations with higher $PM_{2.5}$ concentrations were mainly concentrated in eastern China and CC, and $PM_{2.5}$ pollution was more severe in 2015–17 compared to 2018–19. Li et al. (2020) reported that the concentration of surface O_3 showed consistent increases across China during 2013–19, and continued to rise during 2018–19 even under the Clean Air Action Plan. The continued anthropogenic increase in O_3 may be attributable to the decrease in $PM_{2.5}$ during 2017–19, as well as unmitigated emissions of VOCs.

Figure 3 and Table S1[in the electronic supplementary material (ESM)] show that the occurrence frequency of DHP events increase from 2013 to 2015, and begin to decline from the year 2016. The year 2015 shows the highest frequency, with a total of 269 DHP events, accounting for 16.3% of the total number (1655 DHP events). After 2015, the rates of decline increase first and then decrease, with the smallest in 2015–16 (4.5%) and the largest in 2017–18 (26.1%). The year 2020 shows a minimum of 118 DHP events, accounting for 7.1% of the total number. Although O_3 concentrations show a rising trend during 2018–20 (Li et al., 2020; Zhao et al., 2021; He et al., 2022b), the frequency of DHP events in China still shows a significant decreasing trend, due to a continuous decrease in $PM_{2.5}$ concentrations (Li et al., 2019a, b; Zhai et al., 2019; Zhao et al., 2021). It is also worth mentioning that, due to the stringent policies and lockdown measures implemented during the COVID-19 pandemic, human activities were strictly limited in China, resulting in a 14% decrease in $PM_{2.5}$ concentrations compared with 2019 (Chen et al., 2020b). Thus, the occurrence frequency and region of DHP events decreases in 2020.

In addition, in the monthly statistics of DHP events (Fig. 3 and Table S1 in the ESM), there is an obvious seasonal characteristic. The high frequencies of DHP events occur in the months of March–August, i.e., spring and summer, accounting for 62.6% of all DHP events from 2013 to 2020. (Wang et al. (2015) showed that emissions of NO_x, VOCs, CO, NH_3, OC, and EC have two seasonal peaks during May to June and October, mainly from straw residue burning and fertilizer application, which contribute to the production of both pollutants. Dai et al. (2021) showed that DHP events

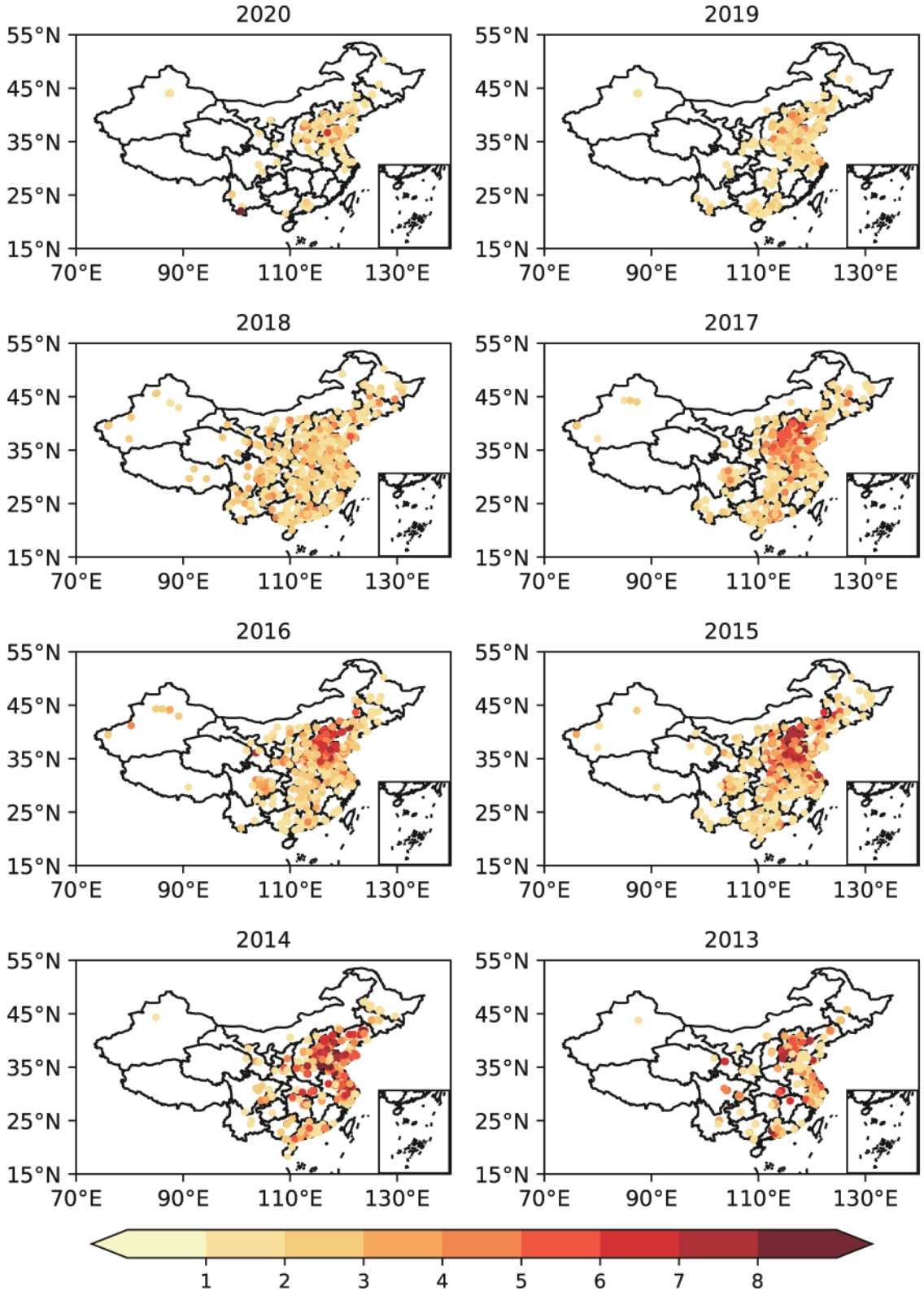

Fig. 2. Site distribution of DHP events in China from 2013 to 2020 and the number of times that DHP events occur over each site.

mainly occurred in April, May, June and October over the YRD during 2015–19. Qin et al. (2021) showed that DHP mostly occurred in spring (April) and autumn (October) over the YRD. Wang et al. (2015) indicated that March–July is a period of agricultural activity, which is not only conducive to the growth and maintenance of $PM_{2.5}$ concentrations but is also a warm period beneficial for the enhancement of O_3 concentrations (Ding et al., 2013). Com-

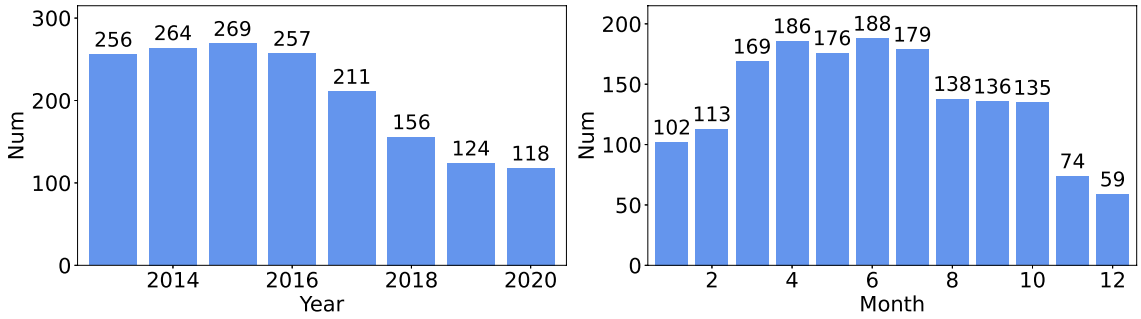

Fig. 3. Yearly and monthly distribution of DHP events in China from 2013 to 2020.

bined with the influence of anthropogenic emissions and favorable meteorological conditions, the frequency of DHP events during this period (March–August) is relatively high.

The frequency of occurrence is relatively low in autumn (345 DHP events; 20.8%) and winter (274 DHP events; 16.6%), but still not negligible. $PM_{2.5}$ concentrations in autumn and winter are severely high under stagnant weather conditions and high anthropogenic emissions (Li et al., 2017; Dang and Liao, 2019). Therefore, DHP events of in autumn and winter mainly depend on the occurrence of abnormally high concentrations of O_3. Some important previous literature has reported that fast O_3 production (to levels exceeding the air quality standard) in wintertime (Schnell et al., 2009; Carter and Seinfeld, 2012; Rappenglück et al., 2014) was driven by high emissions of VOCs and an abrupt decrease in NO_x emissions (due to the Air Pollution Prevention and Control Action Plan targeting $PM_{2.5}$). Extreme VOC concentrations can optimize the O_3 production efficiency of NO_x (Edwards et al., 2014; Li et al., 2021).

3.2. *Main circulation patterns for DHP events over China*

Figure 4 shows the occurrence numbers and proportions of the nine main circulation types obtained by the Lamb–Jenkinson method combined with the ERA5 data for the DHP events of 2013–20 in the five main polluted regions (NCP, YRD, PRD, SCB, and CC) over China. It shows that the occurrence frequencies of A and C types are the highest, accounting for over 40% of the sum of all DHP events, followed by southerly or easterly airflow types like SW, SE, E, and ASE, accounting for over 6%, respectively, over different regions. The rotating airflow types and the flat airflow types can be considered as local synoptic impacts and regional transport, respectively (Yan et al., 2021b). The high occurrence frequency of A and C types indicates the important local contributions to the formation of DHP events over these regions.

The monthly statistics of DHP events for the main circulation types of the five different regions are shown in Fig. S1(in the ESM), indicating various seasonal characteristics. For C type, the numbers of DHP events over these five polluted regions in June–August are significantly higher than those in other months, accounting for 60.9%, 69.0%, 67.4%, 58% of the total in NCP, YRD, PRD, and CC, respectively. Meanwhile, for A type, the numbers of DHP events in non-summer seasons are significantly higher than those in summertime over these five regions, except SCB. The number of DHP events for A type accounts for 31.3% and 37.3% in September–November over the NCP and CC, respectively, but 34.3% in March–May over the YRD, and 49.5% in December–February over the PRD. The meteorological conditions for DHP events controlled by summertime C type and non-summertime A type over these polluted regions are discussed in the following text. In particular, the summertime (June–August) A type–controlled DHP events account for 41.6% over the SCB. Ning et al. (2020) and Zhan et al. (2019) also revealed that, affected by the mountain–basin topography, the synoptic pattern with high pressure (A type) occurring in summer is associated with high levels of air pollution.

Figures 5 and S2–S5 (in the ESM) show the circulation patterns and meteorological conditions of the three major circulation types for DHP events over these five polluted regions averaged over 2013–20. For A type circulation, the NCP, YRD, PRD, and CC are controlled by an anticyclone system at the center of each region and affected by the interaction of a continental high pressure system (CH), the Aleutian low (AL), and WPSH (Fig. 5 and Fig. S2 in the ESM). These four regions at the center of the anticyclone are usually accompanied by sunny and stable weather conditions, which are conducive to photochemical reactions and suppressed diffusion and transport of pollutants (Wang et al., 2017).

For the A type of the NCP region, the intensity of the WPSH (CH) is stronger (weaker), and thus the resultant easterly winds from the East China Sea and southwesterly winds from the Indian Ocean can bring abundant water vapor to Northeast China (Fig. S2a in the ESM). As shown in Fig. S4 and Fig. S5 (in the ESM), the NCP shows high temperatures (regional average: 287.4 K, which is 0.4 K higher than the average value over 2013–20) and high humidity (55.3%, which is 2.4% higher than the average). Such meteorological conditions not only promote more primary pollutants to be converted into secondary pollutants, but also favor both the hygroscopic growth of $PM_{2.5}$ components and the formation of O_3 (Dai et al., 2021). Similarly, for the PRD, the intensity of the AL is much stronger, and the overall position of the systems is southward and the shape of the WPSH is flatter (Fig. 5k and Fig. S2k in the ESM).

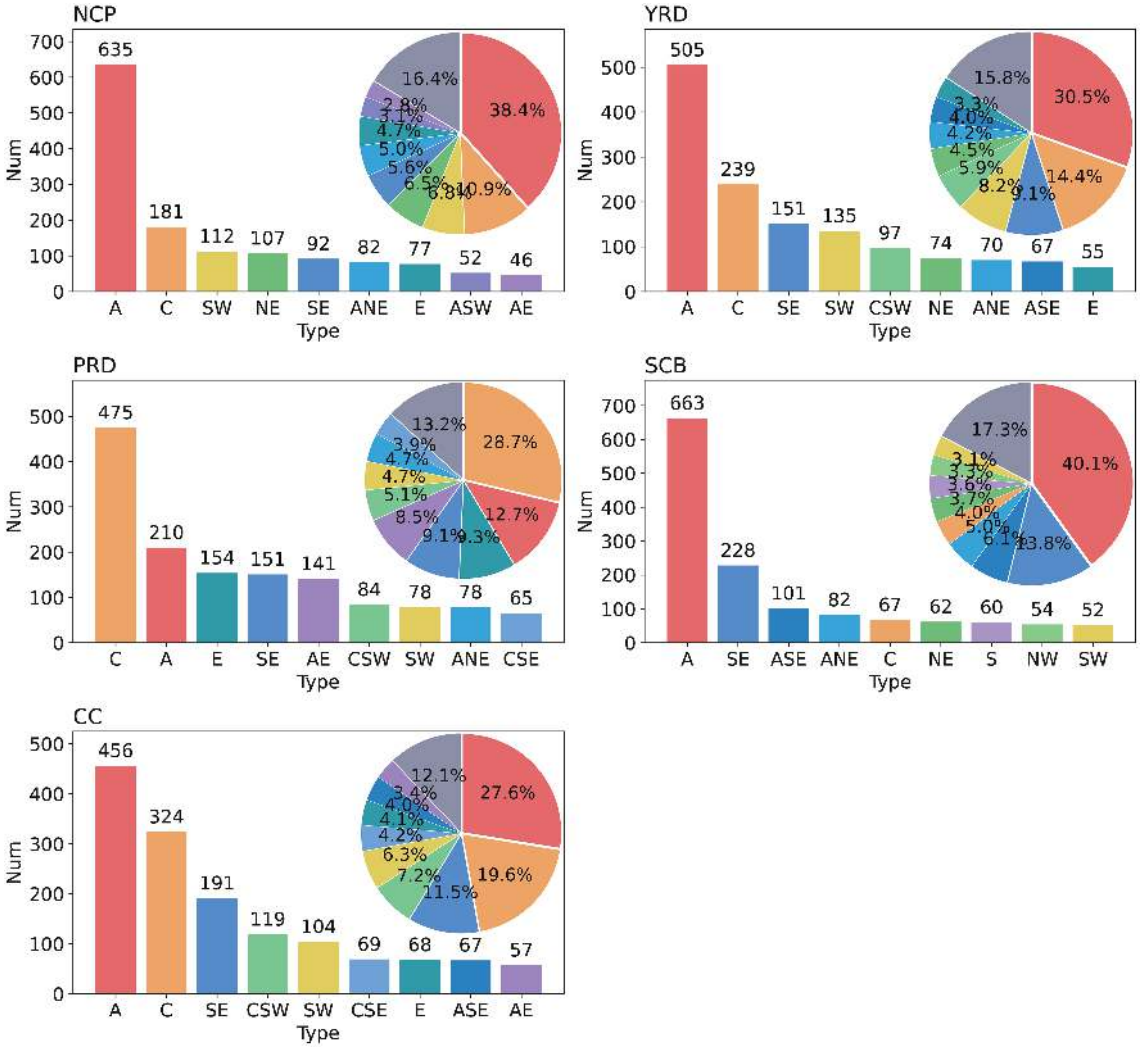

Fig. 4. The occurrence numbers of nine major circulation types and their proportions for the DHP events of 2013–20 over five main polluted regions of China.

For the A type of the YRD region, the CH pressure system is linked together with the WPSH, and a strong and thick AL is located over the Okhotsk Sea, jointly leading to a strong westerly flow over the northeastern part of China (Fig. 5d and Fig. S2d in the ESM). The resultant northwesterly flow hinders the transport of warm and moist air flow from the South China Sea and the East China Sea to the mainland and leads to low temperatures (286.0 K, which is 4.4 K lower than average) and relative humidity (63.9%, which is 8.2% lower than average; Fig. S4 and Fig. S5 in the ESM) in the region. The anticyclone over the YRD is not conducive to the diffusion of pollutants and favors the accumulation of high concentrations of $PM_{2.5}$ and O_3. Similarly, for the A type of the CC region, the results also show low temperatures (289.0 K, which is 2.5 K lower than average) and low relative humidity (58.0%, which is 6.1% lower than average; Fig. S4 and Fig. S5 in the ESM). This is not conducive to the formation of precipitation, making it difficult for pollutants to settle and clear.

In particular, for the A type of the SCB region, its special topography and the influence of the South Asian high jointly lead to the formation of an anticyclone. Over the SCB, the temperature is high (298.2 K, which is 4.2 K higher than average) and the relative humidity is low (76.4%, which 0.7% lower than average; Fig. S4 and Fig. S5 in the ESM). In addition, different from the A type of the other four regions occurring during the cold seasons, the A type of the SCB mainly occurs in the warm seasons.

For C type circulation, compared to A type circulation, the NCP, YRD, PRD, and CC are obviously controlled by a continental low pressure system (CL), and the shape of the WPSH is clearer (Fig. 5 and Fig. S2 in the ESM). The locations of the CL (covering the whole of Eurasia) and WPSH (at around 30° N) for the C type of these four regions are similar. For the PRD, the position of the WPSH shifts eastward, while for the other three regions the western edge of the WPSH extends to the mainland of China. The southwesterly winds on the western ridge of the WPSH combined with the southerly winds from the Indian Ocean can bring abundant water vapor to eastern China. Under the control of C type,

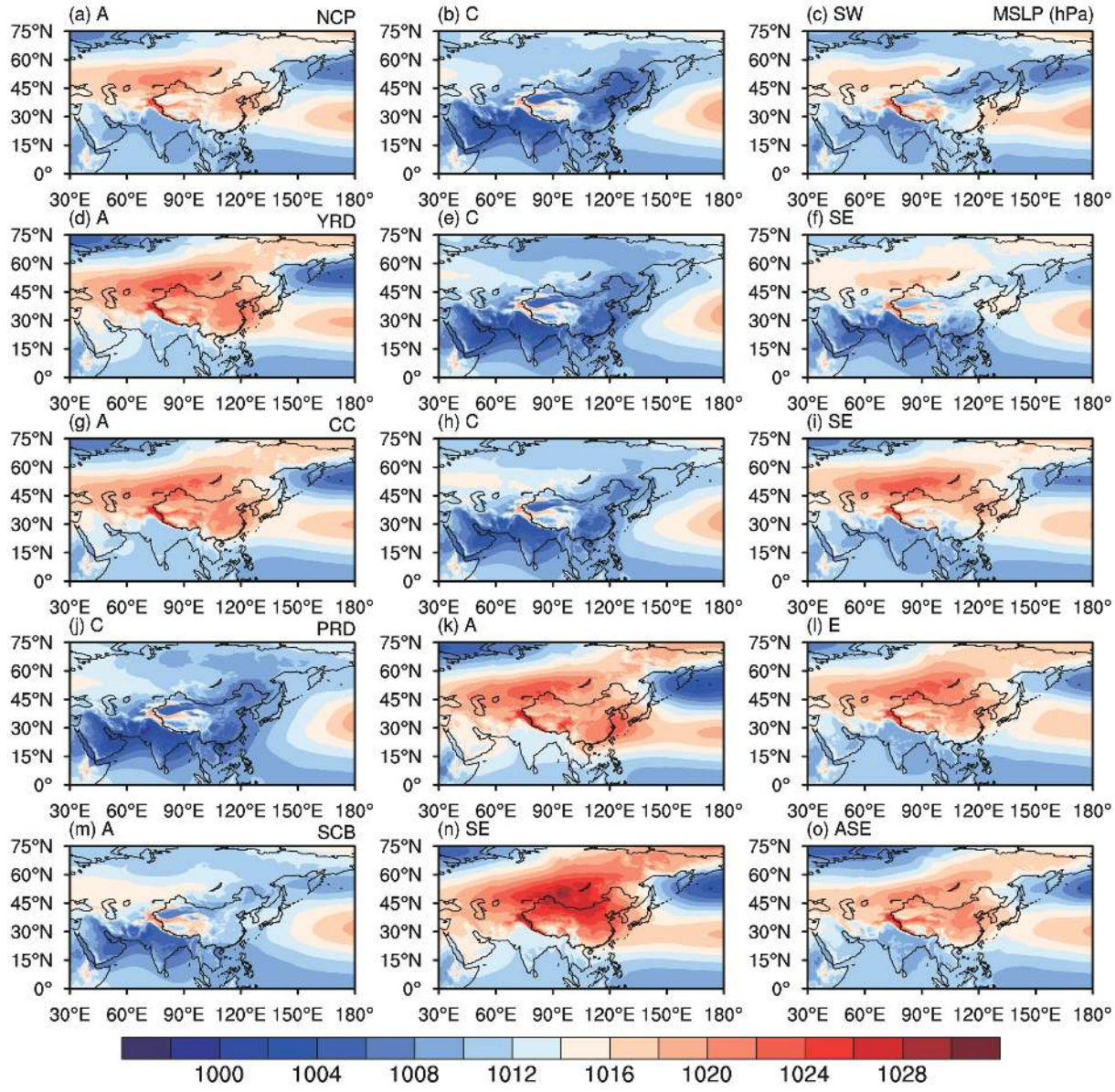

Fig. 5. Spatial distribution of MSLP (units: hPa) of three major circulation types for DHP events over five main polluted regions averaged over 2013–20.

the four regions all show high temperatures (9.3 K, 7.6 K, 6.2 K, and 7.6 K higher than average in the NCP, YRD, PRD, and CC, respectively) and relative humidity (13.8%, 11.4%, 4.7%, and 6.5% higher than average, respectively; Fig. S4 and Fig. S5 in the ESM), which promotes the formation of both $PM_{2.5}$ and O_3.

For the southerly and easterly airflow types (Fig. 5 and Fig. S2), the southerly and easterly airflow can bring water vapor from the ocean to the coastal regions of China (NCP, YRD, PRD, etc.). Thus, the temperature and relative humidity are higher in the coastal regions (Fig. S4 and Fig. S5 in the ESM). For the SE and ASE types of the SCB, with the strong intensity of the CH and the mountain–basin topography, the meteorological conditions show low temperatures and high relative humidity, thus hindering the diffusion of pollutants (Fig. S4 and Fig. S5 in the ESM).

3.3. *Meteorological and chemical causes of DHP events*

3.3.1. *Meteorological causes*

We further analyze the continuous changes of meteorological elements and chemical compositions during DHP events (18 May, 2 and 3 November 2017) that occurred in Wuhan, an essential megacity over CC, to reveal the generation and elimination processes of DHP events.

From 14 to 18 May, the horizontal trough at 500 hPa across the middle and high latitudes of China gradually turns vertical, becomes shallow and shifts eastward (Fig. S6 in the ESM). In addition, the intensity of the WPSH and CL strengthen, and the CL gradually invades mainland China, leading to the eastward movement of the AL. Thus, the winds over CC change from northerly to southerly (Fig. 6 and Fig. S7 in the ESM). Affected by such changes in atmo-

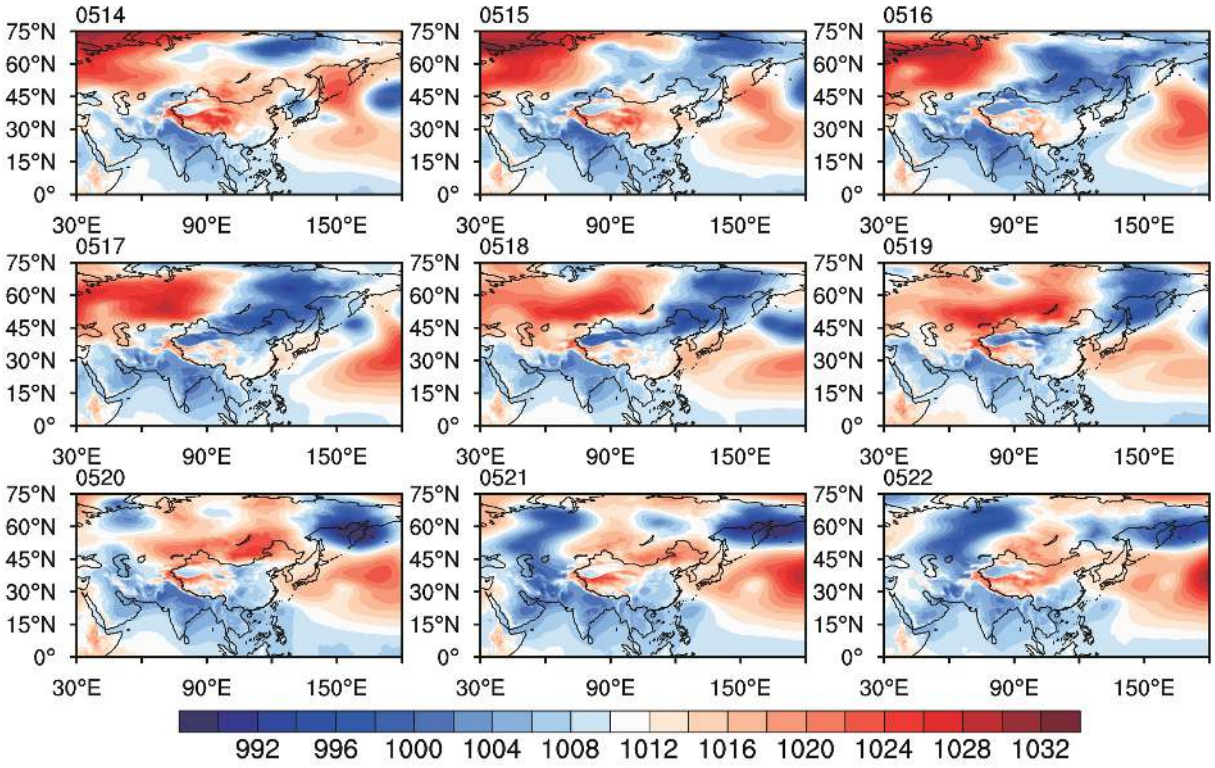

Fig. 6. Spatial distribution of MSLP (units: hPa) from 14 to 22 May 2017.

spheric circulation, the relative humidity over CC decreases and the temperature increases (Fig. S8 and Fig. S9, Table S2, in the ESM). On 18 May, the synoptic type is CSW, which is a mixed type. The warm and dry air is brought from the southwest airflow to Wuhan and stays owing to the cyclone. Wuhan experiences high temperatures (299.4 K, which is 2.8 K higher than the previous five-day average) and low humidity (57.6%, which is 9.6% lower than average). The precipitation over CC from 14 to 15 May might have a certain deposition effect on pollutants (Fig. S10 in the ESM), which restrains the formation of DHP. However, with the reduced cloud cover (not shown), the solar radiation at the surface in Wuhan reaches 753.6 kJ m^{-2} (179.1 kJ m^{-2} higher than average; Table S2 in the ESM), which is conducive to photochemical reactions and promotes the formation of $PM_{2.5}$ and O_3.

From 18 to 22 May, with the eastward shift of the trough at 500 hPa, the westerly wind belt is flatter at high latitudes in China, while several shallow troughs and ridges still appear over CC (Fig. S6 in the ESM). Moreover, the intensity of the Siberian high strengthens, while the CL gradually weakens and moves eastward. Eventually, the CL merges with the AL and strengthens together with the WPSH (Fig. 6 and Fig. S7 in the ESM). Also, with the four days of consecutive precipitation (Fig. S10 in the ESM), the deposition of pollutants accelerates, resulting in declining concentrations of $PM_{2.5}$ and O_3.

From 29 to 31 October, a strong anticyclone forms over CC. In addition, the intensity of the WPSH weakens and moved eastward, the CH is weaker, and the intensity of the AL increases. However, on 1–2 November, the AL weakens while the WPSH and CH strengthen (Fig. 7 and Fig. S11 in the ESM). On 2 November, at 500 hPa, a deep trough forms over CC (Fig. S12 in the ESM), where the convection is weak and not conducive to the diffusion of pollutants. On 3 November, a strong anticyclone is generated over CC at 850 hPa (Fig. S11 in the ESM). Controlled by the anticyclone, the corresponding downdraft makes the water vapor content and cloud cover decrease. Thus, the O_3 concentration increases under strong solar radiation (Fig. S13 to Fig. S16 in the ESM). Moreover, it is also not conducive to the diffusion and spread of pollutants. During this process, both the temperature and relative humidity increase over CC (Table S2 in the ESM). In particular, on 2 November, Wuhan shows low pressure (1019.3 hPa, which is 4.6 hPa lower than the previous five-day average value), high temperature (292.5 K, which is 3.6 K higher than average), and high humidity (60.9%, which is 11.6% higher than average). Coupled with the absence of precipitation, low-cloud cover, and strong solar radiation (450.7 kJ m^{-2} at the surface in Wuhan) (Table S2 in the ESM), photochemical reactions are promoted. It is worth mentioning that, on 2 and 3 November, the synoptic types are E and AE, respectively. Wuhan is surrounded by mountains on three sides, and its eastern side is dotted with factories (Zhang et al., 2015). The eastern airflow type will undoubtedly aggravate pollution in Wuhan.

From 3 to 6 November, associated with the strengthened CH over Eurasia, the CL at high latitudes weakens while the AL strengthens. Finally, the CH moves eastward and

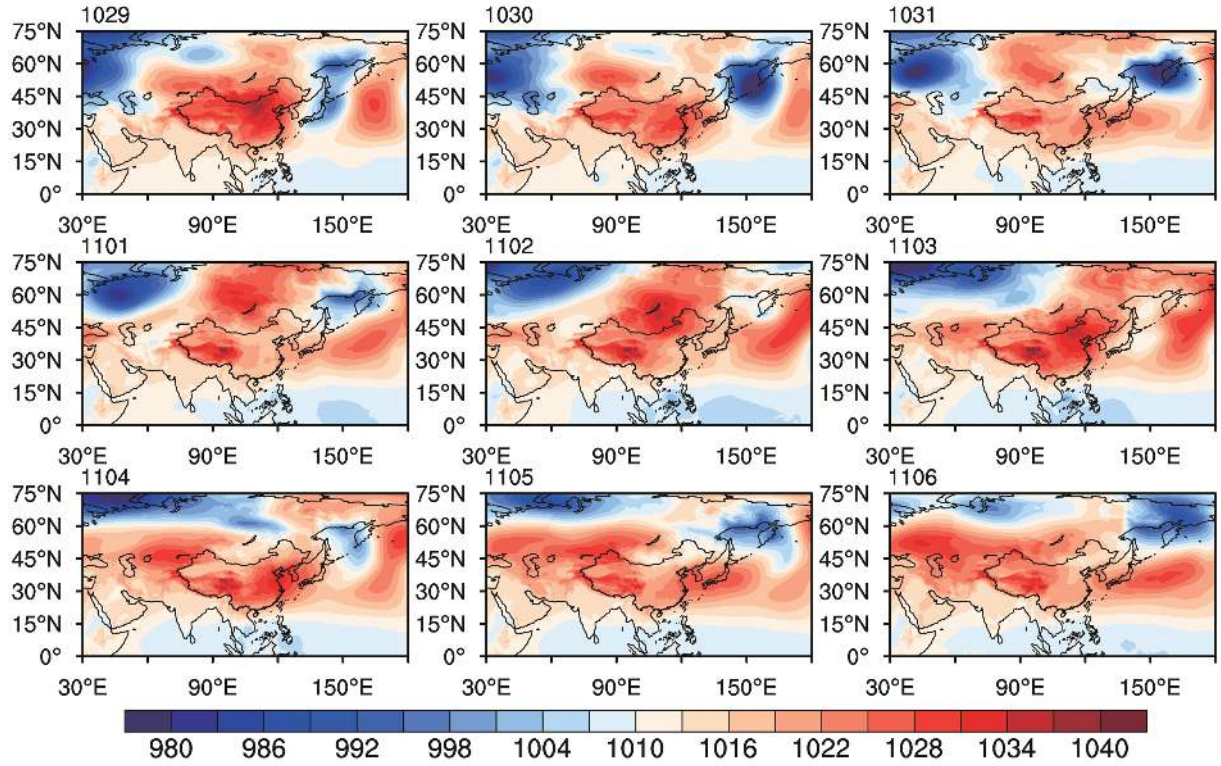

Fig. 7. Spatial distribution of MSLP (units: hPa) from 29 October to 6 November 2017.

merges with the WPSH squeezed by the AL. Affected by the WPSH, a strong southerly flow forms over CC, which promotes the dissipation of pollution (Fig. 7 and Fig. S11 in the ESM).

In addition, observational data in Wuhan (Fig. 8, Fig. 9, Table S3 in the ESM) further show that the meteorological conditions during the DHP event are of still or weak wind (average wind speed: 0.4 m s^{-1}; the wind speed is 0 m s^{-1} for more than half the time; lower than the average value of 0.8 m s^{-1} during non-DHP events), high temperatures (23.1°C, which is 2.2°C higher than average), low humidity (64.9%, which is 5.1% lower than average), and low pressure (1009.1 hPa, which is 1.2 hPa lower than average). The optimal meteorological conditions usually appear in the afternoon at around 1600 LST (Local standard time, LST=UTC + 8 hours), when the O_3 concentration peaks (Fig. 8 and Fig. S17 in the ESM).

3.3.2. *Chemical composition characteristics*

The diurnal cycles of $PM_{2.5}$ and O_3 concentrations show different profiles. As shown in Fig. 8, on 18 May, the concentration of $PM_{2.5}$ reaches a peak of 139 μg m^{-3} at 0500 LST, after which the concentration exhibits a "U" shape, with its minimum value of 34 μg m^{-3} at 1700 LST. However, the concentration of O_3 is at a low level before 0600 LST, and it begins to rise gradually after sunrise at 0600 LST, with its peak value of 198 μg m^{-3} occurring at 1900 LST. Meanwhile, the concentrations of VOCs and NO_x, which are common precursors of $PM_{2.5}$ and O_3, reach a peak of 87.7 and 64 μg m^{-3}, respectively. On 2 November (Fig. S17), the "U" shape of $PM_{2.5}$ concentration reaches a peak of 132 μg m^{-3} at 2300 LST and a minimum value of 57 μg m^{-3} at 1100 LST. Meanwhile, the O_3 concentration reaches the maximum value of 162 μg m^{-3} at 1900 LST, when the NO_2 concentration reaches a peak of 171 μg m^{-3}, and decreases together with NO_2.

SIAs (NO_3^-, SO_4^{2-}, and NH_4^+), carbonaceous substances (OC, EC), and crustal elements (Mg, Al, K, Ca, and Fe) constitute the main components of $PM_{2.5}$ in Wuhan (Zhang et al., 2015; Huang et al., 2019). Consistent with $PM_{2.5}$, the diurnal cycle of the particle concentrations (SIAs, OC, EC, and crustal elements) show maximum values at 0800 LST and minimum values at around 1600 LST, after which the concentrations begin to slowly rebound (Fig. 8). This indicates that the conversion of primary pollutants to secondary components is promoted under the favorable meteorological conditions (subsection 3.3.1), leading to the enhancement of total particle concentrations during the morning.

The concentrations of precursors (NO_2, SO_2, and VOCs) show higher values during the DHP events (daily averages: 62.7 μg m^{-3}, 8.5 μg m^{-3}, and 95.4 ppb, respectively) than those of the following two non-DHP days (daily averages: 54.5 μg m^{-3}, 8.1 μg m^{-3}, and 91.6 ppb, respectively; Fig. 9 and Table S3 in the ESM). As shown in Fig. 8, the concentrations of the three precursors reach their minimums of 22 μg m^{-3} (NO_2), 5 μg m^{-3} (SO_2), and 48.5 ppb (VOCs), and rise at 1600 LST.

As shown in previous studies, meteorological conditions characterized by high relative humidity and low temperature are more conducive to the formation of $PM_{2.5}$ pollution

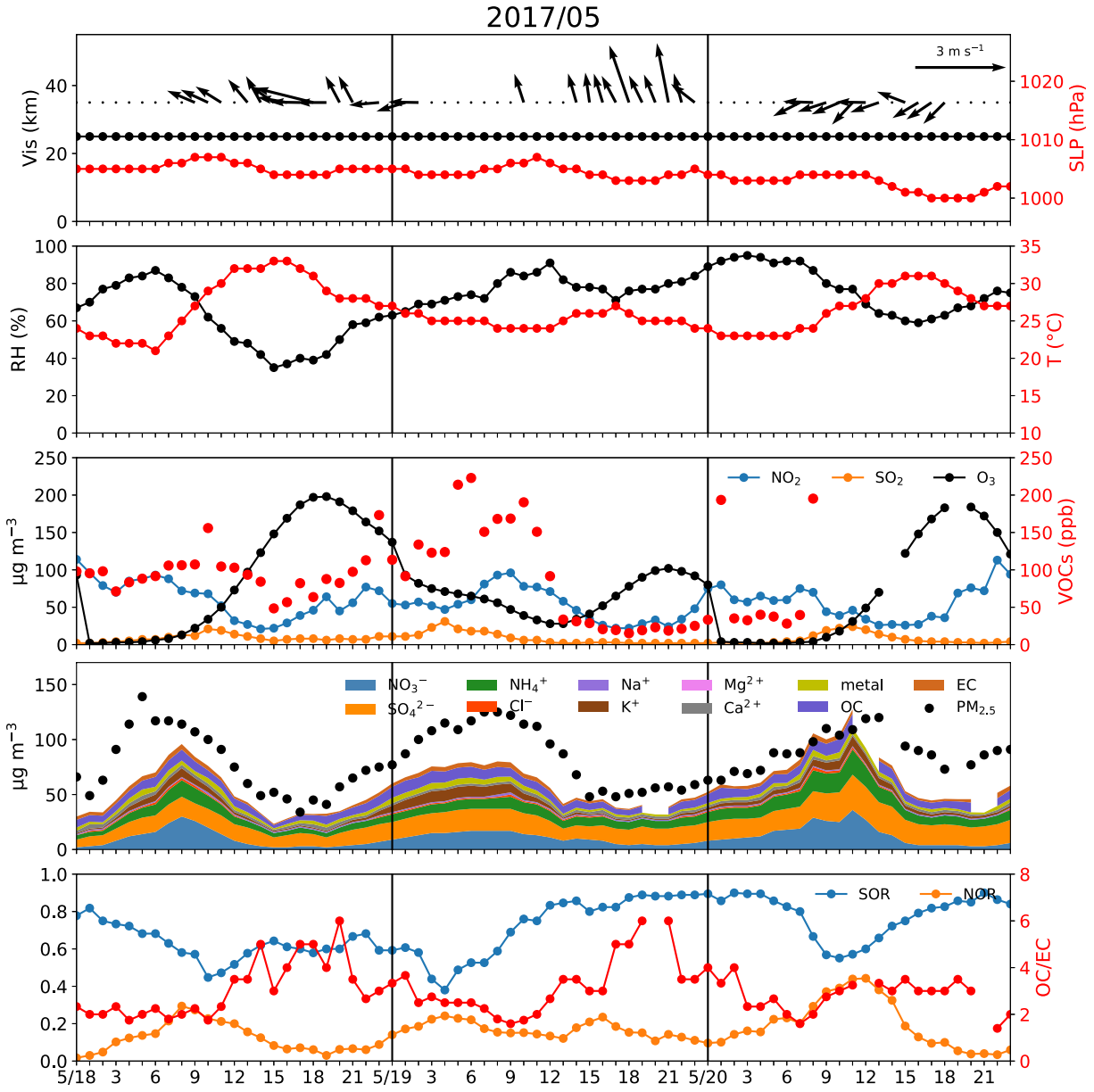

Fig. 8. Meteorological conditions and chemical compositions of Wuhan from 18 to 20 May 2017. The first and second rows present the meteorological conditions, including the visibility (units: km), SLP (units: hPa), wind speed (units: m s^{-1}), wind direction, relative humidity (%) and temperature (units: °C). The third row shows the concentrations of O_3 (units: μg m^{-3}) and three precursors: NO_2, SO_2 (units: μg m^{-3}) and VOCs (units: ppb). The fourth row shows the concentrations of $PM_{2.5}$ and its chemical components, including SIAs, carbonaceous substances, crustal elements, etc. (units: μg m^{-3}). The last row shows three indices related to the transformation rates of primary precursors to secondary aerosols.

(Chen et al., 2020a; Zhao et al., 2020; Ma et al., 2021). In this study, the variations of temperature and relative humidity before and after sunrise during DHP events are more obvious than during the following two non-DHP days (Fig. 8 and Fig. S17 in the ESM). In the morning before sunrise for DHP events, with lower temperature and higher relative humidity, it is more favorable for NO_2 and SO_2 to absorb moisture and transform into NO_3^- and SO_4^{2-}, which corresponds to the high values of NOR and SOR during the same time. However, as the sun rises, the planetary boundary layer height increases and the wind speed accelerates, which promotes the dilution and diffusion of air pollutants (Zhang et al., 2015; Chen et al., 2020a; Zhao et al., 2020), contributing to the decrease in $PM_{2.5}$ concentrations after sunrise.

Also, meteorological conditions characterized by lower relative humidity and higher temperature after sunrise during DHP events are more favorable for the formation of O_3 (Chen et al., 2020a; Zhao et al., 2020; Ma et al., 2021). With the gradual strengthening of radiation intensity, photochemical reactions are further promoted and the concentration of O_3 increases (Fig. 8). Until around 1600 LST, the radiation intensity decreases, the temperature drops, the reaction rate gradually slows, and particles finally enter the accumulation period again (Fig. 8).

Although the formation of high concentrations of $PM_{2.5}$ and O_3 is dominated by different meteorological conditions, the diurnal cycles of meteorological conditions cause $PM_{2.5}$ (0300–1200 LST) and O_3 (1500–2100 LST) to exceed the national standards at different times of the DHP day (Fig. 8).

As shown in Table S3 (in the ESM), the values of SOR and NOR in May (mean value of 0.71 and 0.16, respectively) are significantly higher than those in November (mean value of 0.26 and 0.10, respectively). The diurnal variation of $PM_{2.5}$ concentrations can fit well with the variation of SOR and NOR values (Fig. 8 and Fig. S17 in the ESM), indicating that the conversion to secondary pollutants (SO_4^{2-} and NO_3^-) is important for the formation of $PM_{2.5}$. It can be seen that the OC/EC values increase significantly after 0900 LST during the DHP event; and after 1200 LST as the radiation intensity increases, the value of OC/EC is consistently greater than 2 and even reaches a maximum value of 6, before then beginning to decrease after sunset (Fig. 8 and Fig. S17 in the ESM).

The concentrations of $PM_{2.5}$ are high before sunrise, while the concentrations of O_3 are high after sunrise. Although exhibiting different diurnal cycles, the two kinds of high-concentration pollutants jointly lead to reaching the national standard for DHP on the same day (Fig. S18 in the ESM).

In addition, comparing the pollution conversion indices of consecutive DHP events and non-DHP events in May (Fig. 8, Fig. 9, and Table S3 in the ESM), we can see that even after the DHP event, the conversion rate of primary pollutants is still increasing during subsequent consecutive days. The conversion rates of SOR, NOR, and OC/EC during non-DHP events increase by 14.3%, 41.7%, and 5.6%, respectively. However, the concentrations of precursors (VOCs) during non-DHP events is lower than that during the DHP event (Fig. 9, Table S3 in the ESM), and thus the O_3 concentrations do not exceed the national standard on 19–20 May.

4. Conclusions and implications

In this paper, we analyze the spatial and temporal distribution characteristics of $PM_{2.5}$ and O_3 DHP events in China from 2013 to 2020. Using the Lamb–Jenkinson circulation classification method, we classify the main circulation types of DHP events over five main polluted regions and analyze their effects on the formation of DHP in detail. The meteorological causes and the chemical composition characteristics during the DHP events over CC are also discussed. Ultimately, we draw the following conclusions:

The DHP events (1655 in total in 2013–20) mainly occur in the NCP, YRD, PRD, SCB, and CC. The occurrence frequency increases by 5.1% over 2013–15, and then decreases by 56.1% over 2015–20. The main circulation types of DHP events are C and A, accounting for over 40% of all DHP events over the five main polluted regions, followed by southerly or easterly flat airflow types like SE, SW, and E. Compared with non-DHP events, DHP events are characterized by static or weak winds, high temperatures (20.9°C versus 23.1°C) and low humidity (70.0% versus 64.9%). Under such meteorological conditions, the concentrations of NO_2, SO_2 and VOCs decrease by 13.1%, 4.7% and 4.4%, respectively, after the DHP events, indicating their rapid secondary conversion during DHP events. Although exhibiting different diurnal cycles, these two high-concentration pollutants jointly lead to reaching the national standard for DHP on the same day.

This paper provides a broad view of the spatiotemporal distribution of DHP events in China from 2013 to 2020. The results on the meteorological causes can help in predicting the occurrence of DHP events according to representative con-

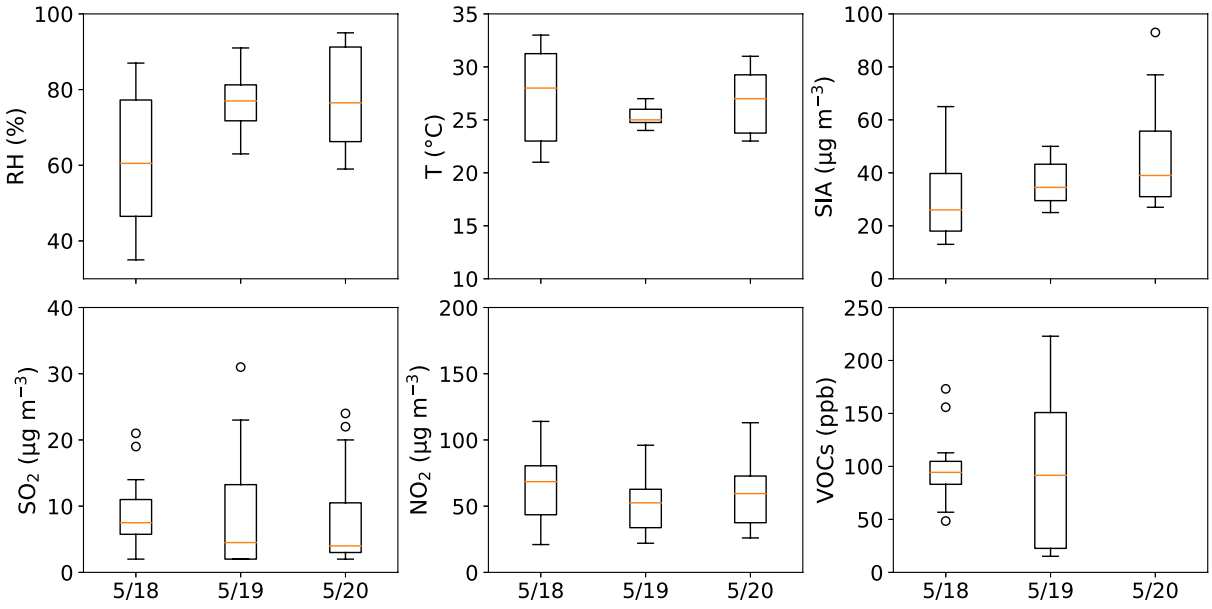

Fig. 9. Boxplots of meteorological conditions and chemical compositions in Wuhan during 18–20 May 2017.

ditions or circulation types. The analysis of the chemical components over CC reveals the diurnal cycles that lead to DHP on a particular day, and the results remind us that we should pay more attention to DHP events. In CC, to reduce the frequency of DHP events, it is necessary to provide early warning of weather conditions that may lead to DHP events, and to continue to strengthen the control of endogenous pollution. However, the chemical causes of DHP events over China are still unclear. To clarify the chemical causes of DHP, further analysis of the sources and effects of $PM_{2.5}$ and O_3 precursors is needed. Subsequent studies should also examine the influence of anthropogenic sources on the formation of DHP.

Acknowledgements. This study was financially supported by the National Natural Science Foundation of China (Grant Nos. 41830965 and 41905112), the Key Program of the Ministry of Science and Technology of the People's Republic of China (Grant No. 2019YFC0214703), and the Hubei Natural Science Foundation (Grant No. 2022CFB027). It was also supported by the State Key Laboratory of Atmospheric Boundary Layer Physics and Atmospheric Chemistry (Grant No. LAPC-KF-2023-07) and the Key Laboratory of Atmospheric Chemistry, China Meteorological Administration (Grant No. 2023B08).

Authors Contributions Zhixuan TONG: Methodology, Investigation, Data curation, Writing - original draft. Yingying YAN: Conceptualization, Methodology, Writing - review & editing. Shaofei KONG: Supervision, review & editing. Jintai LIN: Supervision, review & editing. Nan CHEN: Data curation. Bo ZHU: Data curation. Jing Ma: Data curation. Tianliang ZHAO: Supervision. Shihua QI: Supervision.

Competing Interests The authors declare that they have no known competing financial interests or personal relationships that could have appeared to influence the work reported in this paper.

Availability of data and materials Hourly in situ observation data (2013–20) were obtained from China's Ministry of Ecology and Environment (https://air.cnemc.cn/). The hourly MSLP data and hourly meteorological (ERA5) data at different altitudes from 2013 to 2020 were downloaded from https://www.ecmwf.int/en/forecasts/dataset/ecmwf-reanalysis-v5/. The observed hourly meteorological data and chemical components of DHP events over Wuhan were obtained from the Hubei Atmospheric Superstation Network Integrated Analysis Platform (http://59.172.208.250:8082/).

Electronic supplementary material: Supplementary material is available in the online version of this article at https://doi.org/10.1007/s00376-023-3156-9.

REFERENCES

Brauer, M., and Coauthors, 2016: Ambient air pollution exposure estimation for the global burden of disease 2013. *Environ. Sci. Technol.*, **50**(1), 79−88, https://doi.org/10.1021/acs.est.5b03709.

Carter, W. P. L., and J. H. Seinfeld, 2012: Winter ozone formation and VOC incremental reactivities in the Upper Green River Basin of Wyoming. *Atmos. Environ.*, **50**, 255−266, https://doi.org/10.1016/j.atmosenv.2011.12.025.

Chen, L., J. Zhu, H. Liao, Y. Yang, and X. Yue, 2020a: Meteorological influences on $PM_{2.5}$ and O_3 trends and associated health burden since China's clean air actions. *Science of the Total Environment*, **744**, 140837, https://doi.org/10.1016/j.scitotenv.2020.140837.

Chen, Q. X., C. L. Huang, Y. Yuan, and H. P. Tan, 2020b: Influence of COVID-19 event on air quality and their association in Mainland China. *Aerosol and Air Quality Research*, **20**(7), 1541−1551, https://doi.org/10.4209/aaqr.2020.05.0224.

Dai, H. B., J. Zhu, H. Liao, J. D. Li, M. X. Liang, Y. Yang, and X. Yue, 2021: Co-occurrence of ozone and $PM_{2.5}$ pollution in the Yangtze River Delta over 2013−2019: Spatiotemporal distribution and meteorological conditions. *Atmospheric Research*, **249**, 105363, https://doi.org/10.1016/j.atmosres.2020.105363.

Dang, R. J., and H. Liao, 2019: Severe winter haze days in the Beijing–Tianjin–Hebei region from 1985 to 2017 and the roles of anthropogenic emissions and meteorology. *Atmospheric Chemistry and Physics*, **19**, 10 801−10 816, https://doi.org/10.5194/acp-19-10801-2019.

Ding, A. J., and Coauthors, 2013: Ozone and fine particle in the western Yangtze River Delta: An overview of 1 yr data at the SORPES station. *Atmospheric Chemistry and Physics*, **13**(11), 5813−5830, https://doi.org/10.5194/acp-13-5813-2013.

Edwards, P. M., and Coauthors, 2014: High winter ozone pollution from carbonyl photolysis in an oil and gas basin. *Nature*, **514**(7522), 351−354, https://doi.org/10.1038/nature13767.

Fleming, Z. L., and Coauthors, 2018: Tropospheric Ozone Assessment Report: Present–day ozone distribution and trends relevant to human health. *Elementa: Science of the Anthropocene*, **6**, 12, https://doi.org/10.1525/elementa.273.

He, Y. P., L. Li, H. L. Wang, X. Q. Xu, Y. M. Li, and S. J. Fan, 2022a: A cold front induced co–occurrence of O_3 and $PM_{2.5}$ pollution in a Pearl River Delta city: Temporal variation, vertical structure, and mechanism. *Environmental Pollution*, **306**, 119464, https://doi.org/10.1016/j.envpol.2022.119464.

He, Z. M., P. F. Liu, X. X. Zhao, X. W. He, J. F. Liu, and Y. J. Mu, 2022b: Responses of surface O_3 and $PM_{2.5}$ trends to changes of anthropogenic emissions in summer over Beijing during 2014−2019: A study based on multiple linear regression and WRF–Chem. *Science of the Total Environment*, **807**,150792, https://doi.org/10.1016/j.scitotenv.2021.150792.

Hersbach, H., and Coauthors, 2020: The ERA5 global reanalysis. *Quart. J. Roy. Meteor. Soc.*, **146**(730), 1999−2049, https://doi.org/10.1002/qj.3803.

Hou, X. W., B. Zhu, K. R. Kumar, and W. Lu, 2019: Inter–annual variability in fine particulate matter pollution over China during 2013−2018: Role of meteorology. *Atmos. Environ.*, **214**, 116842, https://doi.org/10.1016/j.atmosenv.2019.116842.

Huang, F., J. B. Zhou, N. Chen, Y. H. Li, K. Li, and S. P. Wu, 2019: Chemical characteristics and source apportionment of $PM_{2.5}$ in Wuhan, China. *Journal of Atmospheric Chemistry*, **76**(3), 245−262, https://doi.org/10.1007/s10874-019-09395-0.

Huang, M., Z. Q. Gao, S. G. Miao, and X. Z. Xu, 2016: Characteristics of sea breezes over the Jiangsu coastal area, China. *Inter-*

national Journal of Climatology, **36**(12), 3908–3916, https://doi.org/10.1002/joc.4602.

Huang, R. J., and Coauthors, 2014a: High secondary aerosol contribution to particulate pollution during haze events in China. *Nature*, **514**(7521), 218–222, https://doi.org/10.1038/nature13774.

Huang, X. F., H. Yun, Z. H. Gong, X. Li, L. Y. He, Y. H. Zhang, and M. Hu, 2014b: Source apportionment and secondary organic aerosol estimation of $PM_{2.5}$ in an urban atmosphere in China. *Science China Earth Sciences*, **57**(6), 1352–1362, https://doi.org/10.1007/s11430-013-4686-2.

Jenkinson, A. F., and F. P. Collison, 1977: An initial climatology of gales over the North Sea. Preprints, Synoptic Climatology Branch Memorandum, No. 62. Bracknell, Meteoro-logical Office.

Lamb, H. H., 1950: Types and spells of weather around the year in the British Isles: Annual trends, seasonal structure of the year, singularities. *Quart. J. Roy. Meteor. Soc.*, **76**, 393–429, https://doi.org/10.1002/qj.49707633005.

Li, B. W., and Coauthors, 2019a: Characterization of VOCs and their related atmospheric processes in a central Chinese city during severe ozone pollution periods. *Atmospheric Chemistry and Physics*, **19**(1), 617–638, https://doi.org/10.5194/acp-19-617-2019.

Li, J., H. Y. Du, Z. F. Wang, Y. L. Sun, W. Y. Yang, J. J. Li, X. Tang, and P. Q. Fu, 2017: Rapid formation of a severe regional winter haze episode over a mega-city cluster on the North China Plain. *Environmental Pollution*, **223**, 605–615, https://doi.org/10.1016/j.envpol.2017.01.063.

Li, K., D. J. Jacob, L. Shen, X. Lu, I. De Smedt, and H. Liao, 2020: Increases in surface ozone pollution in China from 2013 to 2019: Anthropogenic and meteorological influences. *Atmospheric Chemistry and Physics*, **20**(19), 11 423–11 433, https://doi.org/10.5194/acp-20-11423-2020.

Li, K., and Coauthors, 2019b: A two–pollutant strategy for improving ozone and particulate air quality in China. *Nature Geoscience*, **12**(11), 906–910, https://doi.org/10.1038/s41561-019-0464-x.

Li, K., and Coauthors, 2021: Ozone pollution in the North China Plain spreading into the late-winter haze season. *Proceedings of the National Academy of Sciences of the United States of America*, **118**(10), e2015797118, https://doi.org/10.1073/PNAS.2015797118.

Lin, Y. L., J. L. Zou, W. Yang, and C. Q. Li, 2018: A review of recent advances in research on $PM_{2.5}$ in China. *International Journal of Environmental Research and Public Health*, **15**(3), 438, https://doi.org/10.3390/ijerph15030438.

Liu, J. D., and Coauthors, 2019: Quantifying the impact of synoptic circulation patterns on ozone variability in northern China from April to October 2013–2017. *Atmospheric Chemistry and Physics*, **19**(23), 14 477–14 492, https://doi.org/10.5194/acp-19-14477-2019.

Liu, R. Y., Z. W. Ma, Y. Liu, Y. C. Shao, W. Zhao, and J. Bi, 2020: Spatiotemporal distributions of surface ozone levels in China from 2005 to 2017: A machine learning approach. *Environment International*, **142**, 15823, https://doi.org/10.1016/j.envint.2020.105823.

Lu, X., and Coauthors, 2018: Severe surface ozone pollution in China: A global perspective. *Environmental Science & Technology Letters*, **5**(8), 487–494, https://doi.org/10.1021/acs.estlett.8b00366.

Ma, S. M., M. Shao, Y. F. Zhang, Q. L. Dai, and M. J. Xie, 2021: Sensitivity of $PM_{2.5}$ and O_3 pollution episodes to meteorological factors over the North China Plain. *Science of the Total Environment*, **792**, 148474, https://doi.org/10.1016/j.scitotenv.2021.148474.

Mills, G., and Coauthors, 2018: Tropospheric Ozone Assessment Report: Present–day tropospheric ozone distribution and trends relevant to vegetation. *Elementa: Science of the Anthropocene*, **6**, 47, https://doi.org/10.1525/elementa.302.

Monks, P. S., and Coauthors, 2015: Tropospheric ozone and its precursors from the urban to the global scale from air quality to short–lived climate forcer. *Atmospheric Chemistry and Physics*, **15**(15), 8889–8973, https://doi.org/10.5194/acp-15-8889-2015.

Ning, G. C., S. H. L. Yim, Y. J. Yang, F. Gu, and G. H. Dong, 2020: Modulations of synoptic and climatic changes on ozone pollution and its health risks in mountain-basin areas. *Atmos. Environ.*, **240**, 117808, https://doi.org/10.1016/j.atmosenv.2020.117808.

Qian, Y., L. R. F. Henneman, J. A. Mulholland, and A. G. Russell, 2019: Empirical development of ozone isopleths: Applications to los angeles. *Environmental Science & Technology Letters*, **6**(5), 294–299, https://doi.org/10.1021/acs.estlett.9b00160.

Qin, Y., J. Y. Li, K. J. Gong, Z. J. Wu, M. D. Chen, M. M. Qin, L. Huang, and J. L. Hu, 2021: Double high pollution events in the Yangtze River Delta from 2015 to 2019: Characteristics, trends, and meteorological situations. *Science of the Total Environment*, **792**, 148349, https://doi.org/10.1016/j.scitotenv.2021.148349.

Rappenglück, B., and Coauthors, 2014: Strong wintertime ozone events in the Upper Green River Basin, Wyoming. *Atmospheric Chemistry and Physics*, **14**, 4909–4934, https://doi.org/10.5194/acp-14-4909-2014.

Schnell, R. C., S. J. Oltmans, R. R. Neely, M. S. Endres, J. V. Molenar, and A. B. White, 2009: Rapid photochemical production of ozone at high concentrations in a rural site during winter. *Nature Geoscience*, **2**, 120–122, https://doi.org/10.1038/ngeo415.

Shi, G. Q., J. X. Liu, and X. N. Zhong, 2022: Spatial and temporal variations of $PM_{2.5}$ concentrations in Chinese cities during 2015–2019. *International Journal of Environmental Health Research*, **32**, 2695–2707, https://doi.org/10.1080/09603123.2021.1987394.

Wang, L. J., D. Luo, X. L. Liu, J. Q. Zhu, F. L. Wang, B. Li, and L. M. Li, 2021: Effects of $PM_{2.5}$ exposure on reproductive system and its mechanisms. *Chemosphere*, **264**, 128436, https://doi.org/10.1016/j.chemosphere.2020.128436.

Wang, S., G. G. Li, Z. Y. Gong, L. Du, Q. T. Zhou, X. Y. Meng, S. Y. Xie, and L. Zhou, 2015: Spatial distribution, seasonal variation and regionalization of $PM_{2.5}$ concentrations in China. *Science China Chemistry*, **58**(9), 1435–1443, https://doi.org/10.1007/s11426-015-5468-9.

Wang, S. S., and Coauthors, 2019: Chemical characteristics, sources, and formation mechanisms of $PM_{2.5}$ before and during the Spring Festival in a coastal city in Southeast China. *Environmental Pollution*, **251**, 442–452, https://doi.org/10.1016/j.envpol.2019.04.050.

Wang, T., L. K. Xue, P. Brimblecombe, Y. F. Lam, L. Li, and L. Zhang, 2017: Ozone pollution in China: A review of concentrations, meteorological influences, chemical precursors, and effects. *Science of the Total Environment*, **575**, 1582–1596, https://doi.org/10.1016/j.scitotenv.2016.10.081.

Wang, X. L., 2021: Historical air quality data in China. Available from https://quotsoft.net/air. (in Chinese)

Wang, Y. H., and Coauthors, 2020: Contrasting trends of $PM_{2.5}$ and surface–ozone concentrations in China from 2013 to 2017. *National Science Review*, **7**(8), 1331–1339, https://doi.org/10.1093/nsr/nwaa032.

Yan, Y. Y., and Coauthors, 2021a: On the local anthropogenic source diversities and transboundary transport for urban agglomeration ozone mitigation. *Atmospheric Environment*, **245**, 118005, https://doi.org/10.1016/j.atmosenv.2020.118005.

Yan, Y. Y., and Coauthors, 2021b: Effectiveness of emission control in reducing $PM_{2.5}$ pollution in central China during winter haze episodes under various potential synoptic controls. *Atmospheric Chemistry and Physics*, **21**, 3143–3162, https://doi.org/10.5194/acp-21-3143-2021.

Zhai, S. X., and Coauthors, 2019: Fine particulate matter ($PM_{2.5}$) trends in China, 2013–2018: Separating contributions from anthropogenic emissions and meteorology. *Atmospheric Chemistry and Physics*, **19**(16), 11 031–11 041, https://doi.org/10.5194/acp-19-11031-2019.

Zhan, C. C., and Coauthors, 2019: Synoptic weather patterns and their impacts on regional particle pollution in the city cluster of the Sichuan Basin, China. *Atmos. Environ.*, **208**, 34–47, https://doi.org/10.1016/j.atmosenv.2019.03.033.

Zhang, F., Z. W. Wang, H. R. Cheng, X. P. Lv, W. Gong, X. M. Wang, and G. Zhang, 2015: Seasonal variations and chemical characteristics of $PM_{2.5}$ in Wuhan, Central China. *Science of the Total Environment*, **518–519**, 97–105, https://doi.org/10.1016/j.scitotenv.2015.02.054.

Zhao, H., K. Y. Chen, Z. Liu, Y. X. Zhang, T. Shao, and H. L. Zhang, 2021: Coordinated control of $PM_{2.5}$ and O_3 is urgently needed in China after implementation of the "Air pollution prevention and control action plan". *Chemosphere*, **270**, 129441, https://doi.org/10.1016/j.chemosphere.2020.129441.

Zhao, S. P., D. Y. Yin, Y. Yu, S. C. Kang, D. H. Qin, and L. X. Dong, 2020: $PM_{2.5}$ and O_3 pollution during 2015–2019 over 367 Chinese cities: Spatiotemporal variations, meteorological and topographical impacts. *Environmental Pollution*, **264**, 114694, https://doi.org/10.1016/j.envpol.2020.114694.

Zhao, T., L. X. Yang, W. D. Yan, J. M. Zhang, W. Lu, Y. M. Yang, J. M. Chen, and W. X. Wang, 2017: Chemical characteristics of PM_1/$PM_{2.5}$ and influence on visual range at the summit of Mount Tai, North China. *Science of the Total Environment*, **575**, 458–466, https://doi.org/10.1016/j.scitotenv.2016.09.173.

Zheng, B., and Coauthors, 2018: Trends in China's anthropogenic emissions since 2010 as the consequence of clean air actions. *Atmospheric Chemistry and Physics*, **18**(19), 14 095–14 111, https://doi.org/10.5194/acp-18-14095-2018.

Zong, L., and Coauthors, 2021: Large–scale synoptic drivers of co–occurring summertime ozone and $PM_{2.5}$ pollution in eastern China. *Atmospheric Chemistry and Physics*, **21**(11), 9105–9124, https://doi.org/10.5194/acp-21-9105-2021.